Surface-State Spin Textures and Mirror Chern Numbers in Topological Kondo Insulators

Markus Legner, Andreas Rüegg, and Manfred Sigrist
Institut für Theoretische Physik, ETH Zürich, 8093 Zürich, Switzerland
(Received 15 May 2015; published 9 October 2015)

The recent discovery of topological Kondo insulators has triggered renewed interest in the well-known Kondo insulator samarium hexaboride, which is hypothesized to belong to this family. In this Letter, we study the spin texture of the topologically protected surface states in such a topological Kondo insulator. In particular, we derive close relationships between (i) the form of the hybridization matrix at certain high-symmetry points, (ii) the mirror Chern numbers of the system, and (iii) the observable spin texture of the topological surface states. In this way, a robust classification of topological Kondo insulators and their surface-state spin texture is achieved. We underpin our findings with numerical calculations of several simplified and realistic models for systems like samarium hexaboride.

DOI: 10.1103/PhysRevLett.115.156405 PACS numbers: 71.27.+a, 03.65.Vf, 73.20.At, 75.20.Hr

Introduction.—Since the theoretical characterization of topological Kondo insulators (TKIs) [1,2], this class of materials has attracted much attention in the community. One material in particular, samarium hexaboride (SmB_6), has been studied extensively both theoretically and experimentally. Several theoretical studies predicted SmB_6 [3–8] and related compounds [9,10] to be TKIs with protected gapless surface modes. Different experiments showed that, at sufficiently small temperatures, transport is indeed dominated by the surface contributions [11–13]. At the same time, angle-resolved-photoemission-spectroscopy (ARPES) [14–19], quantum-oscillation [20], and scanning-tunneling-microscopy measurements [21] confirmed the existence of gapless surface states. Nevertheless, due to the small bulk gap of 15–20 meV [22–24] and strong electronic correlations, a detailed characterization of the nature of the surface states is difficult and may require additional concepts such as atomic reconstruction [25], Kondo breakdown [26], or excitonic scattering [27]. Some groups also challenged the scenario of a TKI [24,28]. To date, the most conclusive evidence for the topological nature of the surface states is provided by spin-resolved ARPES measurements of the (001) surface [23] showing that the surface states around the $\bar{X}$ point of the surface Brillouin zone (SBZ) are spin-polarized.

SmB_6 is predicted to have a band inversion at the X high-symmetry points (HSPs) [3–6]. The X-inverted phase has a nontrivial strong $\mathbb{Z}_2$ index $\nu_0 = 1$, weak topological indices $\boldsymbol{\nu} = (1,1,1)$, and protected surface Dirac cones as shown in Fig. 1(a) for the (001) surface. The experimental work in Ref. [23] is consistent with these predictions and furthermore suggests that the spin texture of the surface states is as sketched in Fig. 1(c). Interestingly, however, several theoretical studies reached conflicting conclusions about the nature of the spin texture [29–31], which is not uniquely determined by the $\mathbb{Z}_2$ invariants. In fact, for linear Dirac cones, two situations are compatible with the cubic symmetry, see Figs. 1(c) and 1(d). They are distinguished by opposite winding numbers $w_{\bar{X}} = \pm 1$ of the planar unit spin $(n_x, n_y) = (S_x, S_y)/\sqrt{S_x^2 + S_y^2}$ around the $\bar{X}$ point, where the winding number around the HSP $\boldsymbol{K}$ [32] is defined as

$$w_{\boldsymbol{K}} = \frac{1}{2\pi} \oint_{\gamma_{\boldsymbol{K}}} \boldsymbol{\nabla}[\mathrm{Im}\log(n_x + i n_y)] \cdot d\boldsymbol{s}, \qquad (1)$$

with $\gamma_{\boldsymbol{K}}$ a contour encircling $\boldsymbol{K}$ in an anticlockwise fashion. This discrepancy between different theoretical models and approaches raises the important question of what determines the spin texture in cubic TKIs.

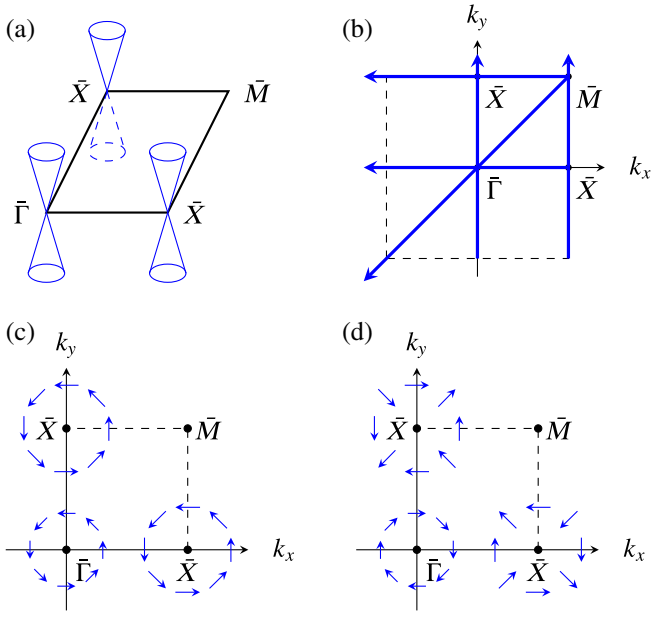

FIG. 1 (color online). (a) Sketch of the Dirac cones in the (001) surface Brillouin zone. (b) Positive directions of mirror invariant lines in the SBZ for the (001) surface with outward pointing normal vector $\boldsymbol{n}_{\mathrm{sf}} = \boldsymbol{e}_z$, see Ref. [33] for further details. (c),(d) Sketch of the spin (or pseudospin, see Sec. II) textures in the (001) SBZ. While at $\bar{\Gamma}$ the winding number is always $w_{\bar{\Gamma}} = 1$, at the $\bar{X}$ points it can be $w_{\bar{X}} = +1$ (c) or $w_{\bar{X}} = -1$ (d), depending on the configuration of the MCNs.

In this Letter, we provide two answers to this question: First, we show that there is a close connection between the spin texture and the mirror Chern numbers (MCNs) [34]. In particular, knowledge of the MCNs allows us to distinguish between the two situations shown in Figs. 1(c) and 1(d). Second, we provide analytical expressions relating the surface-state spin texture to the hybridization parameters of specific models. These relations demonstrate that the number and type of included orbitals in the effective model does *not* uniquely define the winding number; instead, the relative strength of different-range hybridization parameters is equally important. In addition, we show how the system can be tuned across topological phase transitions, during which the surface-state spin texture changes while all the $\mathbb{Z}_2$ invariants remain unaffected.

In the remainder of the Letter, we will provide the details to the above statements. We will also apply the general argumentation to a multiorbital model with itinerant E_g and localized Γ_8 electrons, as in Ref. [31]. Other models are discussed in the Supplemental Material [33].

Mirror Chern numbers define pseudospin texture.—To start, we review certain facts about the MCNs in SmB_6. The MCNs are topological invariants, which are protected by mirror symmetries [8,34,35]. In a cubic system, there are three distinct MCNs: $C_0 \equiv C^{(+i)}_{k_\alpha=0}$, $C_\pi \equiv C^{(+i)}_{k_\alpha=\pi}$, and $C_d \equiv C^{(+i)}_{k_\alpha=k_\beta}$, with $\alpha,\beta \in \{x,y,z\}$ and $\beta \neq \alpha$, where $C^{(+i)}_{\mathcal{S}}$ refers to the Chern number of the Bloch states on the mirror-invariant plane $\mathcal{S}$ with eigenvalue $+i$ under the mirror operation, see also Ref. [35]. As was shown in Ref. [8], the cubic symmetry implies that the MCNs in the X-inverted phase are $C_0 = 2 \bmod 4$, $C_\pi = 1 \bmod 4$, and $C_d = 1 \bmod 2$. These values imply two additional Dirac nodes along the $\bar{\Gamma}\bar{X}$ line on the (110) surface [8,35]. In the following, we show that the MCNs also determine the spin texture on the (001) surface. (A related argument for Hg-based topological insulators was presented in Ref. [36].)

The projections of the mirror planes onto the (001) surface correspond to the high-symmetry lines (HSLs) shown in Fig. 1(b). Along these mirror invariant lines (MILs), we can classify the surface states according to their mirror eigenvalues $\pm i$. The bulk-edge correspondence for each mirror-invariant plane then states that the MCN C is equal to the number of right-moving ($C > 0$) or left-moving ($C < 0$) surface modes with mirror eigenvalue $+i$, see Fig. 2. There exists a certain freedom to choose signs in the calculation of the MCNs. We use a convention [33], which leads to the positive directions shown in Fig. 1(b).

The mirror eigenvalues also define a *pseudospin of the surface states* $\boldsymbol{\mu}$ in the following way: On the $k_y = 0$ or $k_y = \pi$ MIL, we choose a basis $\{\boldsymbol{u}_1, \boldsymbol{u}_2\}$ in which the mirror operator takes the form $M_y = -i\mu_y$, where μ_α is the αth Pauli matrix. Furthermore, on the $k_x = 0$ and $k_x = \pi$ MILs we can choose the mirror operator $M_x = -i\mu_x$. The pseudospin is then given by the spinor $\boldsymbol{u} = a\boldsymbol{u}_1 + b\boldsymbol{u}_2 \equiv (a,b)^{\mathrm{t}}$. Its relation to the physical spin of the electron is detailed in Sec. V. It follows that, along the MILs, the pseudospin lies in the surface plane and is always perpendicular to the MIL. In order to make the connection to the pseudospin texture, it is useful to consider the effective Hamiltonian close to the Dirac node at the HSP $\boldsymbol{K} = \bar{\Gamma}$ or $\boldsymbol{K} = \bar{X}$:

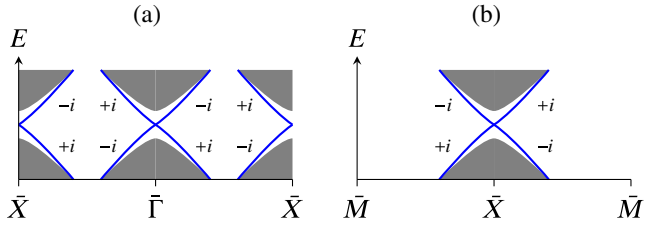

FIG. 2 (color online). Chiral surface states with mirror eigenvalues $\pm i$ along the $\bar{\Gamma}\bar{X}$ (a) and $\bar{X}\bar{M}$ line (b) in positive direction (see Fig. 1) for $C_0 = -2$ and $C_\pi = 1$.

$$H_{\boldsymbol{K}}(\boldsymbol{q}) = v^x_{\boldsymbol{K}}\mu_y q_x - v^y_{\boldsymbol{K}}\mu_x q_y = i(v^x_{\boldsymbol{K}} M_y q_x - v^y_{\boldsymbol{K}} M_x q_y). \quad (2)$$

Here, we measure the momentum relative to the respective HSP, $\boldsymbol{q} = \boldsymbol{k} - \boldsymbol{K}$. At the $\bar{\Gamma}$ point, the cubic symmetry implies that $v^x_{\bar{\Gamma}} = v^y_{\bar{\Gamma}}$ and the resulting pseudospin texture necessarily has a winding number $w_{\bar{\Gamma}} = 1$. But at the $\bar{X}$ points, $v^x_{\bar{X}} \neq v^y_{\bar{X}}$ in general, and the winding number of the pseudospin texture is $w_{\bar{X}} = \mathrm{sgn}(v^x_{\bar{X}} v^y_{\bar{X}})$. Because the MCNs fix the direction of the pseudospin at the points where the Fermi lines cross the MILs, the MCNs also fix the relative sign between $v^x_{\bar{X}}$ and $v^y_{\bar{X}}$ and hence the winding number $w_{\bar{X}}$. It is then easy to see that the set $(C_0, C_\pi) = (2,1)$ implies the pseudospin texture shown in Fig. 1(c), while $(C_0, C_\pi) = (-2,1)$ implies the pseudospin texture shown in Fig. 1(d). For linear Dirac cones at $\bar{\Gamma}$ and $\bar{X}$, there are no other possibilities; i.e., higher MCNs imply additional Dirac nodes along HSLs [33]. (Note that in Fig. 1 we assume a chemical potential above the Dirac nodes.)

Hybridization matrix defines mirror Chern numbers.—We now analyze the connection between microscopic parameters of the electronic Hamiltonian and the set of MCNs. From *ab initio* calculations [5,29,31,37] it is known that the states near the Fermi energy in SmB_6 are predominantly formed by the Sm $5d$ electrons of E_g symmetry and the Sm $4f$ electrons in the $J = 5/2$ multiplet. The latter splits further into a Γ_8 quartet, $|\Gamma^{(1)}_{8,\pm}\rangle = \sqrt{\frac{5}{6}}|\pm\frac{5}{2}\rangle + \sqrt{\frac{1}{6}}|\mp\frac{3}{2}\rangle$ and $|\Gamma^{(2)}_{8,\pm}\rangle = |\pm\frac{1}{2}\rangle$, and a Γ_7 doublet, $|\Gamma_{7,\pm}\rangle = \sqrt{\frac{1}{6}}|\pm\frac{5}{2}\rangle - \sqrt{\frac{5}{6}}|\mp\frac{3}{2}\rangle$, where the index $\pm$ is the *orbital pseudospin* [38]. Our strategy is to start in the trivial insulating phase without band inversion and consider the effective model, which describes the gap closing and subsequent band inversion at the X points.

The little co-group at the X point is isomorphic to the tetragonal symmetry group D_{4h}. Thus, all the irreducible representations are at most two dimensional and the band inversion occurs between the energetically highest single Kramers pair of f electrons $f_{X,\pm}$ and the energetically

lowest single Kramers pair of d electrons $d_{X,\uparrow\downarrow}$. Near the transition between the trivial and the topological phase, the low-energy electronic structure can be obtained from an effective 4×4 Bloch Hamiltonian around the X points,

$$H^X_{\mathrm{eff}}(\boldsymbol{q}) = \begin{pmatrix} \varepsilon^d_{\boldsymbol{q}} & \Phi^\dagger_{\boldsymbol{q}} \\ \Phi_{\boldsymbol{q}} & \varepsilon^f_{\boldsymbol{q}} \end{pmatrix}. \tag{3}$$

Equation (3) is given for a spinor $\psi = (d_{X,\uparrow}, d_{X,\downarrow}, f_{X,+}, f_{X,-})^{\mathrm{t}}$ and $\boldsymbol{q}$ is measured from X. The simultaneous presence of inversion and time-reversal symmetry allows us to choose the hybridization matrix in the form $\Phi_{\boldsymbol{q}} = i\boldsymbol{\phi}_{\boldsymbol{q}}\cdot\boldsymbol{\sigma}$, with $\boldsymbol{\phi}_{\boldsymbol{q}} = \boldsymbol{\phi}^*_{\boldsymbol{q}} = -\boldsymbol{\phi}_{-\boldsymbol{q}}$ and $\boldsymbol{\sigma}$ the Pauli matrices in spin space. In the following, we consider $X = (0,0,\pi)$, and expand to lowest order in $\boldsymbol{q}$: $\varepsilon^d_{\boldsymbol{q}} = \varepsilon_d\mathbb{1}$, $\varepsilon^f_{\boldsymbol{q}} = \varepsilon_f\mathbb{1}$ and

$$\Phi_{\boldsymbol{q}} = i[\phi_1(\sigma_x q_x + \sigma_y q_y) + \phi_2\sigma_z q_z]. \tag{4}$$

As we show below, the relative sign between the two independent parameters ϕ_1 and ϕ_2 of the linearized hybridization matrix [Eq. (4)] determines the set of MCNs and hence the surface-state spin texture in the X-inverted phase.

First, we address the MCN C_0 and therefore consider the mirror plane $k_x = 0$. The mirror operator in the basis of Eq. (3) is $M_x = -i\tau_z\otimes\sigma_x$. Thus, in the subspace $M_x = +i$, Eq. (3) reduces to

$$H^{(+i)}_{\mathrm{eff},k_x=0}(\boldsymbol{q}) = \bar{\varepsilon}\mathbb{1} - \phi_1 q_y\mu_x + \phi_2 q_z\mu_y - \Delta\mu_z, \tag{5}$$

where μ_α are the Pauli matrices acting on the basis vectors $(1,-1,0,0)/\sqrt{2}$ and $(0,0,1,1)/\sqrt{2}$ and we have defined $\bar{\varepsilon}\equiv\frac{1}{2}(\varepsilon_d+\varepsilon_f)$ and $\Delta\equiv\frac{1}{2}(\varepsilon_f-\varepsilon_d)$. The total Berry flux contribution of the lower band of a Dirac model $h(\boldsymbol{k}) = \epsilon(\boldsymbol{k})\hat{\boldsymbol{d}}(\boldsymbol{k})\cdot\boldsymbol{\mu}$ with $\hat{\boldsymbol{d}} = \boldsymbol{d}/|\boldsymbol{d}|$ is

$$C^{\mathrm{Dirac}} = \frac{1}{4\pi}\int dk_1 dk_2 \hat{\boldsymbol{d}}(\boldsymbol{k})\cdot\left(\frac{\partial\hat{\boldsymbol{d}}}{\partial k_1}\times\frac{\partial\hat{\boldsymbol{d}}}{\partial k_2}\right), \tag{6}$$

which for our case with $\boldsymbol{d}(\boldsymbol{k}) = (-\phi_1 k_1, \phi_2 k_2, -\Delta)$ leads to

$$C^{\mathrm{Dirac}}_{k_x=0} = \frac{1}{2}\mathrm{sgn}(\Delta\phi_1\phi_2). \tag{7}$$

Therefore, starting from the trivial phase with $\Delta<0$ and creating a band inversion at X ($\Delta>0$) leads to a MCN of $C_0 = 2\mathrm{sgn}(\phi_1\phi_2)$, where the factor 2 comes from the fact that there are two X points in the $k_x = 0$ plane.

The two other MCNs can be calculated analogously, see Ref. [33] for details. We obtain $C_\pi = 1$ and $C_d = \nu\mathrm{sgn}(\phi_1\phi_2)$, where $\nu = -1$ for a band inversion between (x^2-y^2) and a linear superposition of $\Gamma_8^{(1)}$ and Γ_7, and $\nu = 1$ for a band inversion between $(3z^2-r^2)$ and $\Gamma_8^{(2)}$. Hence, if $\mathrm{sgn}(\phi_1\phi_2) = 1$ (-1), we recover the set of MCNs which imply the pseudospin texture in Fig. 1(c) [Fig. 1(d)]. In general, we obtain

$$w_{\bar{X}} = \mathrm{sgn}(\phi_1\phi_2). \tag{8}$$

Model calculations for SmB_6.—In the following, we will illustrate our theoretical findings by calculations with an effective lattice model for SmB_6. In the interest of simplicity, we will restrict ourselves to the Γ_8 quartet for f electrons and study a model similar to that used in Refs. [3,31]. Analogous calculations can be performed for the full or the Γ_7 model [33]. The Bloch Hamiltonian is an 8×8 matrix

$$H_{(\Gamma_8)} = \begin{pmatrix} h_d & {\Phi_8}^\dagger \\ \Phi_8 & h_8 \end{pmatrix}, \tag{9a}$$

where the hopping of d and f electrons and the hybridization are given by

$$h_d(\boldsymbol{k}) = \sigma_0\begin{pmatrix} -\frac{3}{2}(c_1+c_2)(t_d^{(1)}+2t_d^{(2)}c_3) & \frac{\sqrt{3}}{2}(c_1-c_2)(t_d^{(1)}-2t_d^{(2)}c_3) \\ \frac{\sqrt{3}}{2}(c_1-c_2)(t_d^{(1)}-2t_d^{(2)}c_3) & -4t_d^{(2)}c_1c_2 - 2t_d^{(1)}c_3 - \frac{1}{2}(c_1+c_2)(t_d^{(1)}+2t_d^{(2)}c_3) \end{pmatrix}, \tag{9b}$$

$$h_8(\boldsymbol{k}) = \sigma_0\begin{pmatrix} \epsilon_8 - \frac{3}{2}(c_1+c_2)(t_8^{(1)}+2t_8^{(2)}c_3) & \frac{\sqrt{3}}{2}(c_1-c_2)(t_8^{(1)}-2t_8^{(2)}c_3) \\ \frac{\sqrt{3}}{2}(c_1-c_2)(t_8^{(1)}-2t_8^{(2)}c_3) & \epsilon_8 - 4t_8^{(2)}c_1c_2 - 2t_8^{(1)}c_3 - \frac{1}{2}(c_1+c_2)(t_8^{(1)}+2t_8^{(2)}c_3) \end{pmatrix}, \tag{9c}$$

$$\Phi_8(\boldsymbol{k}) = -i\begin{pmatrix} 3/2V_8^{(1)}(s_1\sigma_1+s_2\sigma_2) + 3V_8^{(2)}[(c_1+c_2)s_3\sigma_3 + c_3(s_1\sigma_1+s_2\sigma_2)]\ldots \\ -\sqrt{3}/2V_8^{(1)}(s_1\sigma_1-s_2\sigma_2) + \sqrt{3}V_8^{(2)}[(c_1-c_2)s_3\sigma_3 + c_3(s_1\sigma_1-s_2\sigma_2)]\ldots \\ -\sqrt{3}/2V_8^{(1)}(s_1\sigma_1-s_2\sigma_2) + \sqrt{3}V_8^{(2)}[(c_1-c_2)s_3\sigma_3 + c_3(s_1\sigma_1-s_2\sigma_2)] \\ V_8^{(1)}[2s_3\sigma_3 + 1/2(s_1\sigma_1+s_2\sigma_2)] + V_8^{(2)}[(c_1+c_2)s_3\sigma_3 + 4(c_2s_1\sigma_1+c_1s_2\sigma_2) + c_3(s_1\sigma_1+s_2\sigma_2)] \end{pmatrix}, \tag{9d}$$

with the Pauli matrices σ_α acting in spin space and the spinor $\psi = (d_{x^2-y^2,\uparrow\downarrow}, d_{3z^2-r^2,\uparrow\downarrow}, f_{\Gamma_8^{(1)},\pm}, f_{\Gamma_8^{(2)},\pm})^{\mathrm{t}}$. Here, $c_\alpha\equiv\cos k_\alpha$ and $s_\alpha\equiv\sin k_\alpha$, and we use $t^{(1,2)}$ ($V^{(1,2)}$) to denote first and second neighbor hopping (hybridization) parameters, respectively. The hopping and hybridization parameters should be considered as renormalized due to a strong local Coulomb interaction for the f electrons [39–41]. As long as the electronic states near the Fermi energy are well described by quasiparticles, the adopted single-particle approach to compute the topological invariants is justified, even in the presence of strong electron correlations [42–44]. A typical band structure in the X-inverted phase (without hybridization) is shown in Fig. 3(a).

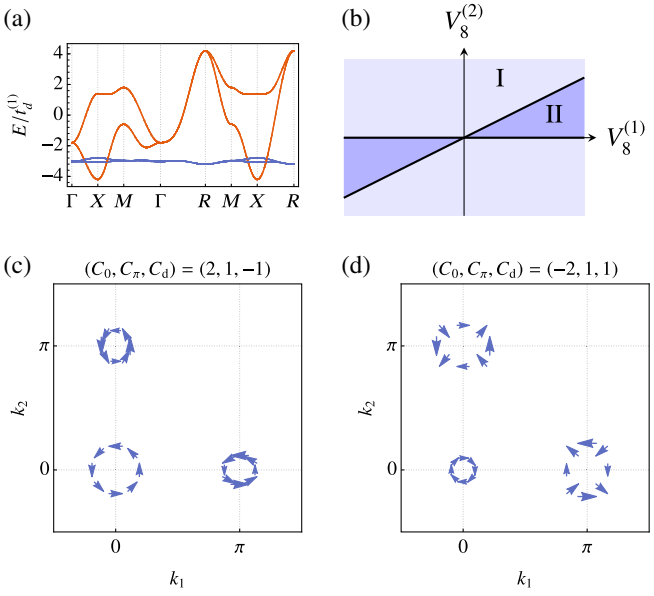

FIG. 3 (color online). Band structure without hybridization (a) and phase diagram (b) for the Γ_8 model defined in Eq. (9) with $t_d^{(1)} = 1$, $t_d^{(2)} = -0.2$, $t_8^{(1)} = -0.03$, $t_8^{(2)} = 0.02$, and $\epsilon_8 = -3$. The two spin textures [(c),(d)] in phases I and II, respectively, are realized for the hybridization parameters $(V_8^{(1)}, V_8^{(2)}) = (0.3, 0.07)$ and $(V_8^{(1)}, V_8^{(2)}) = (-0.1, 0.1)$, respectively.

For $k_x = \pm k_y$, the off-diagonal elements of both h_d and h_8 vanish and the d and f electrons are split into $(x^2 - y^2)$ and $(3z^2 - r^2)$ orbitals, and $\Gamma_8^{(1)}$ and $\Gamma_8^{(2)}$, respectively. Therefore, at the point $X = (0, 0, \pi)$ we obtain

$$h_d(X) = \sigma_0 \mathrm{diag}[-3(t_d^{(1)} - 2t_d^{(2)}), t_d^{(1)} - 2t_d^{(2)}], \quad (10)$$

and similarly for the Γ_8 orbitals. *Ab initio* calculations [9] suggest that $t_d^{(1)}, t_8^{(2)} > 0$ and $t_d^{(2)}, t_8^{(1)} < 0$, such that the band inversion occurs between the $(x^2 - y^2)$ and the $\Gamma_8^{(1)}$ orbitals. The hybridization matrix for these two orbitals can be expanded to first order at the X point:

$$-i\Phi_{\boldsymbol{q}} = \frac{3}{2}(\sigma_x q_x + \sigma_y q_y)(V_8^{(1)} - 2V_8^{(2)}) - 6V_8^{(2)}\sigma_z q_z. \quad (11)$$

Therefore, according to Eq. (8), we obtain

$$w_{\bar{X}} = -\mathrm{sgn}[V_8^{(2)}(V_8^{(1)} - 2V_8^{(2)})], \quad (12)$$

leading to the phase diagram shown in Fig. 3(b). As discussed above, $\nu = -1$ for $(x^2 - y^2)$ and $\Gamma_8^{(1)}$ orbitals, such that we expect $(C_0, C_\pi, C_d) = (2, 1, -1)$ in phase I, leading to a pseudospin texture with $w_{\bar{X}} = 1$, while we expect $(C_0, C_\pi, C_d) = (-2, 1, 1)$ and $w_{\bar{X}} = -1$ in phase II. At the phase transitions $V_8^{(2)} = 0$, the hybridization vanishes along the ΓX line, for $V_8^{(2)} = \frac{1}{2}V_8^{(1)}$ it vanishes at both the XM and XR lines. This causes the hybridization gap to close and the MCNs (C_0, C_π, C_d) to change by $(\pm 4, 0, \mp 2)$. We numerically confirmed the phase diagram in Fig. 3(b) by directly calculating the MCNs using a method for a discretized BZ [45]. Figures 3(c) and 3(d) show the *physical-spin* texture in phases I and II, respectively. They were calculated for a slab of 500 unit cells and fit the expected texture for the *pseudospin*.

Relation between physical spin and pseudospin.—The observed equivalence between physical spin and pseudospin texture in Fig. 3 requires more attention: Because the f electrons experience strong spin-orbit coupling, the orbital pseudospin defined above is not equivalent to the physical spin of the electrons and the mirror and spin operators do not commute. The relation between physical spin and orbital pseudospin for the $J = 5/2$ multiplet is given in Ref. [33].

According to the definition of the pseudospin above, a surface pseudospin in positive $\boldsymbol{n}$ direction corresponds to an eigenvalue $-i$ of $M_{\boldsymbol{n}}$. In order to find a relation between the pseudospin and physical-spin texture of the surface states, we therefore consider the effect of the projector $P_{\boldsymbol{n}}^{\mathrm{ps}} \equiv \frac{1}{2}(\mathbb{1} + iM_{\boldsymbol{n}})$ on the physical-spin operator $S_{\boldsymbol{n}}$, where $P_{\boldsymbol{n}}^{\mathrm{ps}}$ projects onto the subspace $M_{\boldsymbol{n}} = -i$ and $\boldsymbol{n}$ is the normal vector of the mirror plane. One can show that, for the E_g and $J = 5/2$ multiplets,

$$P_{\boldsymbol{n}}^{\mathrm{ps}} S_{\boldsymbol{n}'} P_{\boldsymbol{n}}^{\mathrm{ps}} \equiv 0 \quad \text{for } \boldsymbol{n} \perp \boldsymbol{n}', \quad (13)$$

which states that on a MIL, the physical spin is always parallel (or antiparallel) to the surface-state pseudospin. Whether the two are parallel or antiparallel is determined by the eigenvalues of the projected spin operator,

$$S_{\boldsymbol{n}}^{\mathrm{ps}} \equiv P_{\boldsymbol{n}}^{\mathrm{ps}} S_{\boldsymbol{n}} P_{\boldsymbol{n}}^{\mathrm{ps}}. \quad (14)$$

For the d orbitals we have $\boldsymbol{S} = \boldsymbol{\sigma}$ leading to eigenvalues $+1$ of $S_{\boldsymbol{n}}^{\mathrm{ps}}$, while for the Γ_7, the Γ_8, and the full model, we obtain the (approximate) spectra $\{-0.24\}$, $\{0.52, 0.14\}$, and $\{0.71, 0.14, -0.43\}$, respectively, see Ref. [33]. As all eigenvalues are positive for the Γ_8 model, the physical spin is indeed always *parallel* to the surface-state pseudospin and all findings concerning the pseudospin are directly transferable to the physical spin. This is not the case if we also consider the Γ_7 orbital, because the projected spin operator of f electrons also has negative eigenvalues. In these cases, the relation between pseudospin and physical spin of the surface states depends on the orbital character of the state. In all cases we have studied, the *winding number* of the physical spin sufficiently close to the Dirac node is nevertheless identical to the winding number of the pseudospin. However, the direction may be reversed around some of the Dirac points. Indeed, we find that this may occur for the Γ_7 model, signaling a dominant (in terms of spin) Γ_7 character of the surface states [33].

Finally, we mention that for other models with band crossings along some HSLs, there is the possibility of phases with higher MCNs and a larger number of protected surface states. We discuss an example in Ref. [33].

Conclusion.—We have derived a close relationship between the hybridization matrix at the X high-symmetry points, the mirror Chern numbers, and the spin texture of the topologically protected surface states in topological Kondo insulators. Although we have motivated our study with SmB_6, the line of argumentation also applies to other

topological insulators. Explicit calculations for different models for SmB_6 showed that the spin texture of the surface states does not only depend on the orbitals that are included in the effective model, but also depends on the magnitude of different hybridization parameters. This fact needs to be kept in mind when interpreting *ab initio* or effective-model-based calculations for this type of materials. Finally, our results can be used to infer mirror Chern numbers from spin-resolved ARPES measurements and predict further observables.

We would like to thank T. Neupert, M. Shi, and N. Xu for inspiring discussions. This work is financially supported by a grant of the Swiss National Science Foundation.

Note added.—Recently, a related study [46] with compatible results has appeared.

[1] M. Dzero, K. Sun, V. Galitski, and P. Coleman, Phys. Rev. Lett. **104**, 106408 (2010).
[2] M. Dzero, K. Sun, P. Coleman, and V. Galitski, Phys. Rev. B **85**, 045130 (2012).
[3] T. Takimoto, J. Phys. Soc. Jpn. **80**, 123710 (2011).
[4] M.-T. Tran, T. Takimoto, and K.-S. Kim, Phys. Rev. B **85**, 125128 (2012).
[5] F. Lu, J. Z. Zhao, H. Weng, Z. Fang, and X. Dai, Phys. Rev. Lett. **110**, 096401 (2013).
[6] V. Alexandrov, M. Dzero, and P. Coleman, Phys. Rev. Lett. **111**, 226403 (2013).
[7] M. Dzero and V. Galitski, J. Exp. Theor. Phys. **117**, 499 (2013).
[8] M. Ye, J. W. Allen, and K. Sun, arXiv:1307.7191.
[9] X. Deng, K. Haule, and G. Kotliar, Phys. Rev. Lett. **111**, 176404 (2013).
[10] H. Weng, J. Zhao, Z. Wang, Z. Fang, and X. Dai, Phys. Rev. Lett. **112**, 016403 (2014).
[11] S. Wolgast, C. Kurdak, K. Sun, J. W. Allen, D.-J. Kim, and Z. Fisk, Phys. Rev. B **88**, 180405 (2013).
[12] D. J. Kim, S. Thomas, T. Grant, J. Botimer, Z. Fisk, and J. Xia, Sci. Rep. **3**, 3150 (2013).
[13] X. Zhang, N. P. Butch, P. Syers, S. Ziemak, R. L. Greene, and J. Paglione, Phys. Rev. X **3**, 011011 (2013).
[14] H. Miyazaki, T. Hajiri, T. Ito, S. Kunii, and S. I. Kimura, Phys. Rev. B **86**, 075105 (2012).
[15] N. Xu, X. Shi, P. K. Biswas, C. E. Matt, R. S. Dhaka, Y. Huang, N. C. Plumb, M. Radović, J. H. Dil, E. Pomjakushina, K. Conder, A. Amato, Z. Salman, D. M. Paul, J. Mesot, H. Ding, and M. Shi, Phys. Rev. B **88**, 121102 (2013).
[16] M. Neupane *et al.*, Nat. Commun. **4**, 2991 (2013).
[17] J. Jiang, S. Li, T. Zhang, Z. Sun, F. Chen, Z. R. Ye, M. Xu, Q. Q. Ge, S. Y. Tan, X. H. Niu, M. Xia, B. P. Xie, Y. F. Li, X. H. Chen, H. H. Wen, and D. L. Feng, Nat. Commun. **4**, 3010 (2013).
[18] E. Frantzeskakis, N. de Jong, B. Zwartsenberg, Y. K. Huang, Y. Pan, X. Zhang, J. X. Zhang, F. X. Zhang, L. H. Bao, O. Tegus, A. Varykhalov, A. de Visser, and M. S. Golden, Phys. Rev. X **3**, 041024 (2013).
[19] C.-H. Min, P. Lutz, S. Fiedler, B. Y. Kang, B. K. Cho, H.-D. Kim, H. Bentmann, and F. Reinert, Phys. Rev. Lett. **112**, 226402 (2014).
[20] G. Li, Z. Xiang, F. Yu, T. Asaba, B. Lawson, P. Cai, C. Tinsman, A. Berkley, S. Wolgast, Y. S. Eo, D.-J. Kim, C. Kurdak, J. W. Allen, K. Sun, X. H. Chen, Y. Y. Wang, Z. Fisk, and L. Li, Science **346**, 1208 (2014).
[21] M. M. Yee, Y. He, A. Soumyanarayanan, D.-J. Kim, Z. Fisk, and J. E. Hoffman, arXiv:1308.1085.
[22] B. Gorshunov, N. Sluchanko, A. Volkov, M. Dressel, G. Knebel, A. Loidl, and S. Kunii, Phys. Rev. B **59**, 1808 (1999).
[23] N. Xu, P. K. Biswas, J. H. Dil, R. S. Dhaka, G. Landolt, S. Muff, C. E. Matt, X. Shi, N. C. Plumb, M. Radović, E. Pomjakushina, K. Conder, A. Amato, S. V. Borisenko, R. Yu, H.-M. Weng, Z. Fang, X. Dai, J. Mesot, H. Ding, and M. Shi, Nat. Commun. **5**, 4566 (2014).
[24] P. Hlawenka, K. Siemensmeyer, E. Weschke, A. Varykhalov, J. Sánchez-Barriga, N. Y. Shitsevalova, A. V. Dukhnenko, V. B. Filipov, S. Gabáni, K. Flachbart, O. Rader, and E. D. L. Rienks, arXiv:1502.01542.
[25] N. Heming, U. Treske, M. Knupfer, B. Büchner, D. S. Inosov, N. Y. Shitsevalova, V. B. Filipov, S. Krause, and A. Koitzsch, Phys. Rev. B **90**, 195128 (2014).
[26] V. Alexandrov, P. Coleman, and O. Erten, Phys. Rev. Lett. **114**, 177202 (2015).
[27] G. A. Kapilevich, P. S. Riseborough, A. X. Gray, M. Gulacsi, T. Durakiewicz, and J. L. Smith, Phys. Rev. B **92**, 085133 (2015).
[28] Z.-H. Zhu, A. Nicolaou, G. Levy, N. P. Butch, P. Syers, X. F. Wang, J. Paglione, G. A. Sawatzky, I. S. Elfimov, and A. Damascelli, Phys. Rev. Lett. **111**, 216402 (2013).
[29] R. Yu, H. Weng, X. Hu, Z. Fang, and X. Dai, New J. Phys. **17**, 023012 (2015).
[30] J. Kim, K. Kim, C.-J. Kang, S. Kim, H. C. Choi, J.-S. Kang, J. D. Denlinger, and B. I. Min, Phys. Rev. B **90**, 075131 (2014).
[31] P. P. Baruselli and M. Vojta, Phys. Rev. B **90**, 201106 (2014).
[32] The HSP $\boldsymbol{K}$ has the property $-\boldsymbol{K} = \boldsymbol{K} + \boldsymbol{G}$, where $\boldsymbol{G}$ is a reciprocal lattice vector. On the (001) surface, there are three different HSPs: Γ, $\bar{X}$ and $\bar{M}$.
[33] See Supplemental Material at http://link.aps.org/supplemental/10.1103/PhysRevLett.115.156405 for further details of the calculations and additional examples.
[34] L. Fu, Phys. Rev. Lett. **106**, 106802 (2011).
[35] M. Legner, A. Rüegg, and M. Sigrist, Phys. Rev. B **89**, 085110 (2014).
[36] Q.-Z. Wang, S.-C. Wu, C. Felser, B. Yan, and C.-X. Liu, Phys. Rev. B **91**, 165435 (2015).
[37] C.-J. Kang, J. Kim, K. Kim, J. Kang, J. D. Denlinger, and B. I. Min, J. Phys. Soc. Jpn. **84**, 024722 (2015).
[38] This orbital pseudospin should not be confused with the surface-state pseudospin defined before. The detailed relation between the orbital pseudospin and the physical spin of the f electrons is given in the Supplemental Material [33].
[39] N. Read and D. M. Newns, J. Phys. C **16**, L1055 (1983).
[40] P. Coleman, Phys. Rev. B **29**, 3035 (1984).
[41] T. M. Rice and K. Ueda, Phys. Rev. Lett. **55**, 995 (1985).
[42] Z. Wang and S.-C. Zhang, Phys. Rev. X **2**, 031008 (2012).
[43] M. Hohenadler and F. F. Assaad, J. Phys. Condens. Matter **25**, 143201 (2013).
[44] J. Werner and F. F. Assaad, Phys. Rev. B **88**, 035113 (2013).
[45] T. Fukui, Y. Hatsugai, and H. Suzuki, J. Phys. Soc. Jpn. **74**, 1674 (2005).
[46] P. P. Baruselli and M. Vojta, Preceding Letter, Phys. Rev. Lett. **115**, 156404 (2015).